The Prediction of Aeronoise in High-Reynolds Number Flow

Tijmen Ton, t.a.ton@student.utwente.nl

Dennis van Putten, d.s.vanputten@student.utwente.nl

University of Twente, The Netherlands

Bento Silva de Mattos, bmattos@ita.br

Marco Aurélio Ortega, ortega@ita.br

Technological Institute of Aeronautics – Aeronautical Engineering Division, São José dos Campos – SP - Brazil

Abstract. *The present work is concerned with an accurate prediction of complex transient flow with a high degree of flow separation and its associated aeroacoustic field. A benchmark two-dimensional flow simulation for a cylinder as well as for a slatted airfoil were performed. Experience was gained from the benchmark case and used in the 2D airfoil case. An acoustic analogy is employed for the noise prediction. The flow is simulated using Large Eddy Simulation (LES) approach and the acoustic propagation is successively calculated with the Ffowcs Williams and Hawkings method. For the LES a relative fine mesh is required. The time step is limited by the acoustical calculation, the spectrum is calculated for the whole audible range (20-20,000 Hz). Because the high frequencies require a small time step and the low frequencies impose a long total simulated physical time, a lot of timesteps have to be calculated. The acoustical results are found to be overestimated by an amount of 10 dB, although the trend of the spectrum showed good agreement. The peak sound pressure level and its corresponding frequency are predicted very well in the cylinder case. The character of the 2D high-lift airfoil case was dominantly broadband. Mean force coefficients are predicted accurately in the cylinder case, but the fluctuation coefficients were not. In the airfoil case the lift was overpredicted by about 20%. The reason for the global overprediction is thought to be the elementary defect of simulating highly turbulent 3D flow in a 2D fashion. The 2D simulations can be used however, to obtain a global understanding of the flow pattern and how noise is being generated.*

Keywords*: applied aerodynamics, aeroacoustics, aircraft design, computational fluid dynamics*

1. INTRODUCTION

Air traffic is continuously increasing. Because of the growing number of airplanes in the sky, noise problems are, and will become even more a critical issue. Cause of great concern is the aircraft noise signature during the take-off and approach flight phase, because of the low flight altitude over inhabited areas. Airport related restrictions, such as fight scheduling, airport location and steep-approach flight path, only form a small-scale temporary solution to the problem. Therefore, in present-day aircraft design, noise generation is a very important issue. To allow air traffic to grow in the future, while keeping the noise levels within tolerable limits, advances have to be made in aircraft design. Airframe noise during approach phase comes from the landing gear and from high-lift devices, such as flaps and slats (Fig. 1). Most of the airframe noise is broadband in nature, with low-frequency tones associated with cavities and discontinuities. Noise perception is subjective. Humans can sense frequencies between 20 Hz and 20 kHz, but are most disturbed by sound in 2-4 kHz range. Aircraft noise is unique in that it is wide-ranging and variable in frequency, amplitude, and duration. Thus it is considered to be especially annoying to the public.

The strongly unsteady flow around an aircraft raises considerably the noise level. Numerical simulation of aeroacoustics is not yet a mature technique. Direct Numerical Simulation of the full unsteady compressible Navier-Stokes equations

quickly becomes excessively expensive for higher Reynolds numbers. A promising alternative to this method is to use Large Eddy Simulation (LES) to accurately predict the unsteady incompressible flowfield, from which the acoustic field can be calculated using an acoustic analogy approach. Although a lot of effort was put into its development, up to now the results vary in accuracy. Especially for complex flow situations with a high degree of flow detachment, such as blunt body flow, the accuracy of the predictions is not very high. This study aims to investigate the suitability of the LES and acoustic analogy code of the commercial CFD package Fluent for complex flows with a high degree of flow detachment. The final objective of the study is to roughly predict the sound generated by a slatted airfoil configuration. In order to gain understanding of the problems involved with this kind of simulation, the initial effort was directed towards the airflow around a circular cylinder.

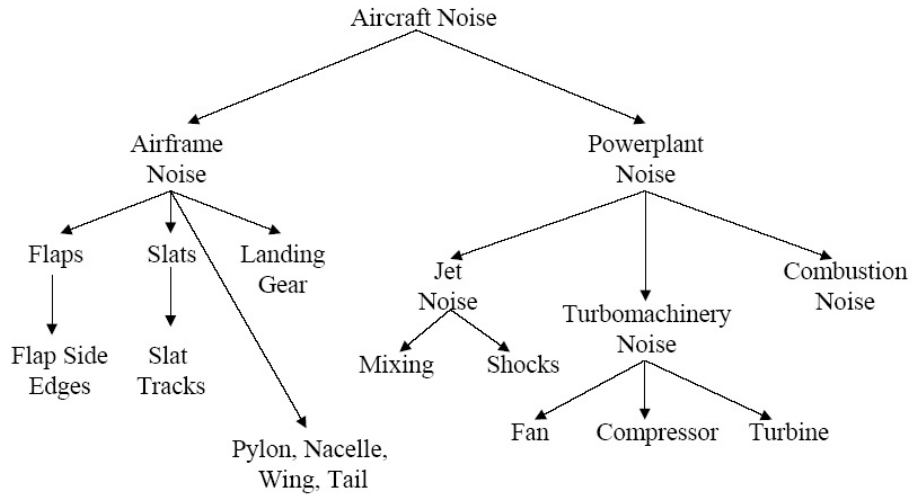

Figure 1 – Subsonic noise sources.

2. DEVELOPMENT

2.1 GRID GENERATION

A proper grid is essential for a simulation with the required accuracy. In this Section the mesh generation is explained. Initially some important mesh parameters are discussed. Then the geometries of the different cases are given and the problem regions are identified. Finally the meshes that will be used for the simulations are presented.

In wall bounded flows it is important to resolve the boundary layer on a high resolution grid. This is because of the high velocity gradient present at the wall. The velocity profile of the boundary layer can be made dimensionless with the viscosity, density and the wall shear by applying (1) to the dimensional wall distance (y) and the dimensional velocity (u).

$$y^+ = \frac{yu_*}{u}, \quad u^+ = \frac{u}{u^*} \tag{1}$$

With

$$u^* = \frac{t_w}{r} \tag{2}$$

For many turbulent wall boundary layers the region near the wall has a universal character. This character can be described by the universal velocity distribution law. This law divides the near wall region in two separate areas, denoted by the viscous sublayer and the log-law zone. The viscous sublayer is the region nearest to the wall. For both regions the relations between the dimensionless variables given in (3) and (4)

$$u^+ = y^+ \text{ (viscous sublayer)} \tag{3}$$

$$u^+ = A \log y^+ + D \text{ (log-law zone)} \tag{4}$$

In the relation for the log-law region the constants A and D are determined experimentally and are given by the respective values 5.85 and 5.56, as found in Schlichting [13]. The dimensionless velocity profile can be plotted and is given in Figure 2. As can be seen the viscous sublayer extends to a y^+ of about 5. As a *rule of thumb* the first node in the boundary layer must be at the location of $y+ \leq 4$ for incompressible flow, see Tannehill [15]. With this value the initial height of the first element on the surface can be determined. Between the viscous sublayer and the log-law region a buffer zone is present in which neither of the descriptions is exactly true. Neglecting this buffer zone, the transition between the regions lies on $y^+ \approx 11.2$.

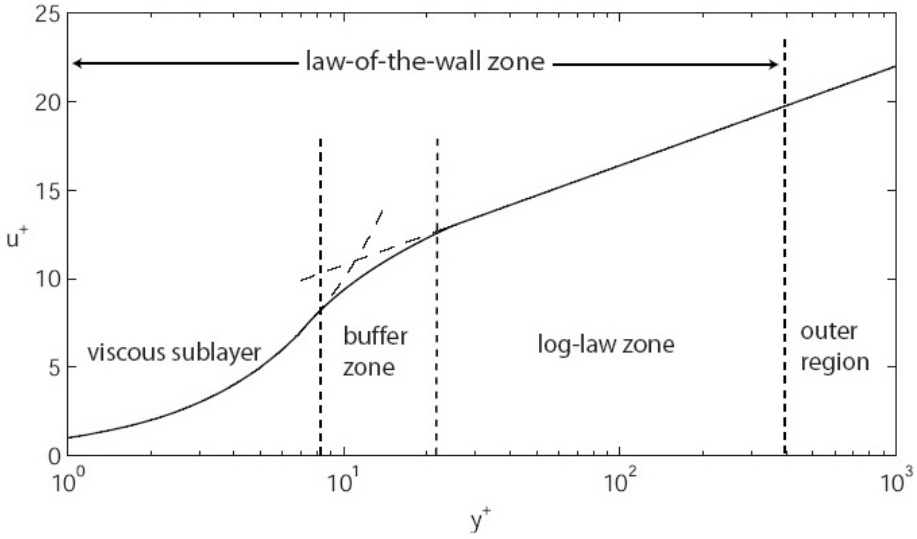

Figure 2 – The relationship between y^+ and u^+.

For flows with high shear stress this *solve-to-wall* approach can lead to a very small initial height of the surface element closest to wall. The computational expense can increase significantly if the boundary layer is to be resolved on a fine grid. An alternative way for simulating the wall bounded flow is making use of the so-called *law-of-the-wall*, which models the universal velocity distribution (shown in Figure 2). This means that the *y*+ value is relieved up to about 30 and the whole region is covered by a wall function. In Fluent the wall function is automatically applied if the *y*+ is located in the log-law region. Although this seems profitable, the use of the wall function is known to be badly suited for flows with boundary layer separation. On the other hand, we also know from literature that LES has difficulties with the *solve-to-wall* approach, because of extremely high grid resolution demands in the near-wall region. The difference between the two approaches was investigated using the cylinder test case.

To obtain all the frequencies in the audible range it is important to know which eddies should still be resolved on the grid and which scales can be modeled by the subgrid-scale model. The smallest eddies that are solved accurately by the LES produce the highest frequency. The relation for calculating the mesh size is therefore related to the highest frequency of interest. It can be read in Colonius [3] that the wave number of turbulence (k_t) is approximately related to the frequency (ω) by

$$k_t = \frac{w}{U_c} \tag{5}$$

where the convection velocity is given by U_c . If all audible sound is to be simulated, the maximum frequency (*fmax*) is about 20 kHz. From the wave number the characteristic eddy length scale can be determined. The frequency emitted by an eddy is related to its length scale (L_t) by (6). Fluent [4] offers a *rule of thumb* for capturing this eddy accurately. They state that the eddy must be solved on 5 grid points.

$$\frac{2p}{L_t} = \frac{w}{U_c} \rightarrow \Delta x = \frac{U_c}{5 f_{\max}} \tag{6}$$

This will result in a grid size of 7 x 10^{-4} m for a characteristic velocity of 70 m/s. This method is based on the wave-length of an eddy. Another way of determining the mesh size is by considering the acoustic wavelength (λ_a) of the highest frequency that has to be resolved on the grid. The acoustic wave number can be determined in the same way as

$$k_a = \frac{w}{c_0} \tag{7}$$

Where c_0 is the speed of sound. By applying the same variables to relation (7), a criterion for the mesh size is found. This relation is given in (8).

$$\Delta x = \frac{c_0}{5 f_{\max}} \tag{8}$$

This will result in a mesh size of 3.4 x 10^{-3} m for the same free stream conditions.

It is clear that the relation for determining the mesh size by considering the eddy length scale is more restrictive than the one calculated by the required acoustic wavelength. The relation between the two restrictions can be expressed in terms of the Mach number, as given in (9). This relation is also derived in Colonius [3]. From this it follows that for low Mach numbers the scale of the smallest turbulent eddies causing audible sound is much smaller than the smallest audible acoustic wavelength.

$$\frac{l_a}{L_t} \propto \frac{1}{M} \tag{9}$$

For the problem of the slatted airfoil configuration the physical domain size is so large in comparison to the mesh size, the resulting mesh will contain so many cells, that performing a simulation will not be feasible because of the limited availability of resources. The mesh size will therefore be increased in agreement with a priori knowledge about the interesting frequency ranges obtained from experimental data.

The restrictions presented above apply to both directions on the surface. However in some three-dimensional configurations the flow structures do not vary much in the spanwise direction for an upswept wing, so it is expected that in these cases some regions on the geometry can be relieved. Several meshes with increasing mesh density are generated. Intuitively the accuracy of the simulation is expected to go up with a decreasing mesh size. Because the wall-treatment adopted by Fluent depends on y+ this is not necessarily true though. Some comparative simulations that be later described in this paper indicates that this approach is better.

For the cylinder case three separate grids will be used. Initially an existing grid from Fluent is used. This grid does not comply with the restrictions necessary for the *solve-to-wall* approach. This means that a wall function is used by Fluent when solving the near-wall region. The mesh is given in Figure 3. It shall be referred to as the coarse mesh.

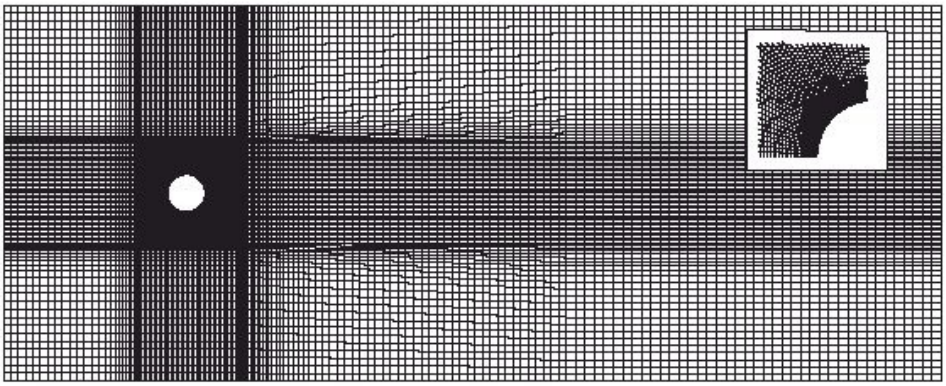

Fig. 3 - Coarse structured mesh for the cylinder case.

The insert shows a detail of the mesh around the cylinder surface. As can be seen the mesh is refined on the cylinder and the lines of the cells are perpendicular to the cylinder surface. The mesh contains about 1.9×10^4 cells with a maximum $y+$ value of about 40. This relatively large mesh size allows a shorter simulation time.

To determine the effects of the wall function, two other meshes are generated with ICEM CFD. One has a maximum $y+$ value of 0.8 and the other a value of 2.5. The boundary layer will therefore be *solved-to-the-wall* for both meshes. They will be referred to as the fine and the intermediate mesh. Both meshes are structurally similar, the difference residing in the element size. The fine mesh is shown in Figure 4.

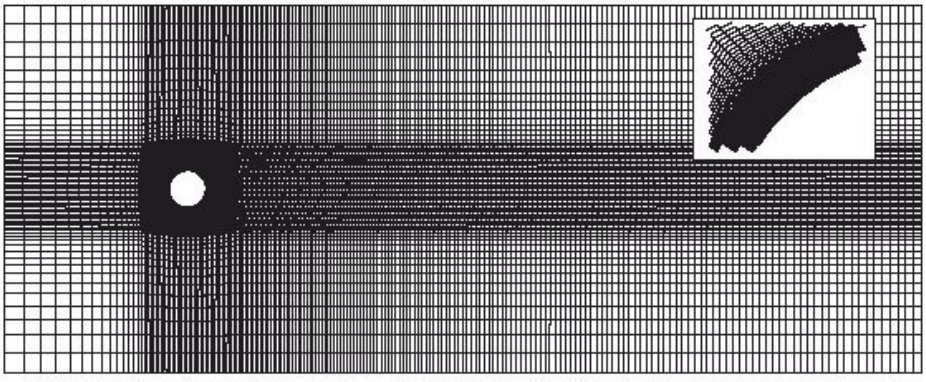

Figure 4 – Fine mesh for the cylinder case.

For aeroacoustical reasons, another mesh is created that contains an additional surface close to the cylinder. This so-called integration surface is a circle with a diameter of 36 mm. Between the surface of the cylinder and the integration surface a fine mesh is chosen to discretize the computational domain in order to prevent dissipation effects becoming larger. A sketch of the location of the integration surface is given in Figure 5.

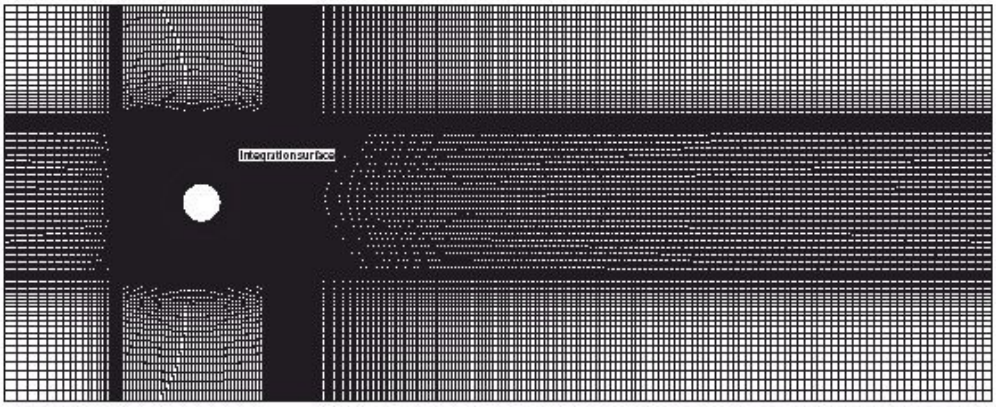

Figure 5 – Cylinder mesh with off-body integration surface.

The slatted-airfoil case is based upon a reference multiple-element airfoil presented by case A-2 in AGARD Advisory Report number 303 [2].

Considerably noise is expected to radiate from the unsteady flow in the slat cove and from the slat trailing edge. Because the configuration consists of two separate surfaces, a new integration surface had to be created to capture the acoustical effects of both the slat and main wing. The integration surface must capture the important sound radiation zones as mentioned before. Substantial differences in slat-generated sound emission were found in a study of Singer et al. [14] when using different integration surfaces. The results suggested that the use of an off-body integration surface containing the slat cove was preferable to an on-body surface. Both on-body and off-body integration surface were investigated in the present work. The mesh size in the slat cove is of the same order as the scale of the eddies of interest. This is done because it is believed that the scheme used in the Fluent package is very diffusive. By taking small elements in this region, acoustical information loss is avoided.

2.2 AERODYNAMIC ANALYSIS

The LES technique is based upon a filtering of the Navier-Stokes equations. The filter is designed to separate the larger eddies from the smaller ones. In most LES applications the small eddies are defined as the eddies that are smaller than the grid size. The large eddies are to be resolved directly, while the small eddies are to be modeled. This modeling, commonly called subgrid-scale modeling, closes the problem. In comparison to Reynolds-Averaged Navier-Stokes (RANS) less of the turbulent field is modeled, more is directly solved. In addition, the part that is modeled can be predicted more accurately. As first proposed by Andrei N. Kolmogorov in 1941, there exists a sort of local isotropy at the smaller scales of turbulence; anisotropy decreases when scales become smaller. This means that small eddies respond more quickly to changes in mean flow properties, so they can be assumed as being in approximate equilibrium with local conditions of the mean flow. This makes the small eddies more suitable for modeling purposes. Another, more intuitive, way of justifying the LES approach, follows from a look at the characteristic energy spectrum of the turbulence scales. In Figure 6 this spectrum is shown, as was presented by Kolmogorov.

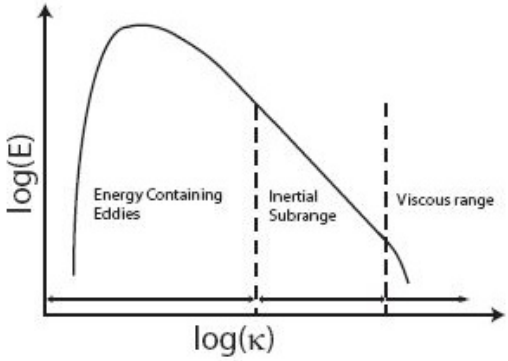

Figure 6 – Energy spectrum of turbulent scales.

As can be seen, the majority of the energy is contained in the larger eddies. The inertial subrange is a domain in which the wave numbers are small of enough that viscosity does not affect motion, but large enough that the overall dimensions of the flow (such as boundary layer thickness) do not matter. At larger wave numbers, in the viscous range, the viscous effects do matter. An estimate of the smallest eddy existing in a flow is provided by the Kolmogorov scale. At this scale, the viscous forces become so large that the eddies dissipate completely. From an energetical point of view, focusing our attention to the larger eddies should give us a smaller error. The energy contained in the small eddies only contributes a small part to the total energy of the flow, thus having less influence on the mean flow pattern. For a more detailed overview of turbulent energy transfer, the reader is referred to Tennekes and Lumley [17]. Some efforts have been made in deriving a more mathematical justification of LES, but these all go beyond the scope of this report. For more information the reader is referred to Guermond et al. [5] and Layton [6].

Fluent features some subgrid models: Smagorinsky model; Wall Adapting Local Eddy-viscosity (WALE) model; Locally Dynamic Smagorinsky (LDS) model; and Locally Dynamic subgrid Kinetic energy transport (LDK) model.

2.3 AEROACOUSTICS MODELING

In modern engineering many ways of computing the acoustical field are used. In this chapter first the possibilities of solving the acoustic field are discussed. In the second part the acoustic theory is explained. Also some practical quantities for measuring the acoustic field are presented.

The possible methods for calculating the acoustical field are given below. Not all methods are available in the Fluent package.

- Computational Aeroacoustics (CAA).
- CFD-wave equation coupling.
- Integral acoustic method.
- Broadband noise source model.

The CAA method is the equivalent of solving the Navier-Stokes equations by means of DNS (Direct Navier-Stokes). In CAA the problems are even bigger because the receiver needs to be within the computational domain, so a very large grid would have to be used if the receiver is located far away from the sound sources. The second method separates the calculation of the flowfield from the calculation of the acoustic field. So first the unsteady flowfield is determined by CFD and these results are fed to a wave equation solver. This implies that there is no coupling between the acoustic waves and the flowfield. If an additional assumption is made, the integral acoustic method is obtained. This method assumes that the receiver has an unobstructed view to each of the individual points that is a source of noise. Also the method does not account for reflections of sound waves on solid boundaries. The most simplified model is the broadband noise source model. This model calculates the sound sources from a synthesized steady state solution, provided by RANS. It is very interesting as industrial tool because it provides quickly a result.

Unfortunately, the accuracy is limited because most of the solution procedure is based on models and not on simulation. The acoustic field of the situations we are considering is dominated by vortex shedding. Furthermore, the configuration consists of several individual parts. This means that the method of CFD-wave equation coupling would be best suited for the calculation of the acoustic field. However, this method is computationally expensive, because again a partial differential equation has to be solved on a grid. For calculations in the farfield this implies a large grid. Besides these considerations, this method requires additional programs that are not available for this study. Therefore, here, the integral acoustic method is the most attractive method for calculating the acoustics. The assumptions made in this method are discussed in the following sections. Both methods are also referred to as Segregated Source-Propagation Methods (SSPM).

2.3.1 LIGHTHILL'S ACOUSTIC ANALOGY

The equation of Lighthill can be derived from the mass and momentum equation. The essence is to work towards a wave equation in which the acoustic source terms are explicitly present. In this derivation the absence of mass sources in the domain is assumed. The mass and momentum equations are then given by

$$\frac{\partial p}{\partial t} + \frac{\partial u_i}{\partial x_i} = 0 \qquad (10)$$

$$\frac{\partial \rho u_i}{\partial t} + \frac{\partial \rho u_i u_j}{\partial x_j} = \frac{\partial s_{ij}}{\partial x_j} + f_i \qquad (11)$$

where s_{ij} is the stress tensor comprising the viscous stresses t_{ij} and the static pressure p (12). The body force in i-direction is given by f_i. For a Newtonian fluid the viscous stress tensor can be written in terms of viscosity and the gradient of the velocity field as stated in (13)

$$s_{ij} = t_{ij} - d_{ij} p \tag{12}$$

$$t_{ij} = m\left(\frac{\partial u_i}{\partial x_j} + \frac{\partial u_j}{\partial x_i} - \frac{2}{3}\frac{\partial u_i}{\partial x_i} d_{ij} \right) \tag{13}$$

If the time derivative of the mass equation and the divergence of the momentum equation are taken, these equations can be combined to obtain equation (14). By linearzing the pressure and the density and subtracting the term $c_0^2 \frac{\partial^2 r'}{\partial x_i \partial x_i}$ from both sides, (14) can be rewritten as (15). The linearization is done around the uniform free field pressure and density. This is only valid for very small perturbations on the free field conditions, which is the case in general acoustics.

$$\frac{\partial^2 r}{\partial t^2} = \frac{\partial^2}{\partial x_i \partial x_j}\left(s_{ij} + r u_i u_j \right) - \frac{\partial f_i}{\partial x_i} \tag{14}$$

$$\frac{\partial^2 r'}{\partial t^2} - c_0^2 \frac{\partial^2 r'}{\partial x_i \partial x_i} = \frac{\partial^2 T_{ij}}{\partial x_i \partial x_j} - \frac{\partial f_i}{\partial x_i} \tag{15}$$

On the left hand side the wave equation is obtained for the perturbation of the density. In this equation the right hand side contains the acoustic source terms. The last term is the contribution of an alternative body force. The T_{ij} is referred to a Lighthill's stress tensor and is given by

$$T_{ij} = r u_i u_j - t_{ij} + \left(p' - c_0^2 r' \right) d_{ij} \tag{16}$$

The three terms of Lighthill's stress tensor those are responsible for the production of sound are:

- $r u_i u_j$, related to non-linear convective forces;
- t_{ij}, viscous forces;
- $\left(p' - c_0^2 r' \right) d_{ij}$, deviation from sound speed or isotropic behavior.

A more complete description of Lighthill's acoustic analogy can be read in Lighthill [7]. The form presented in (15) can be used for a wave equation solver.

2.3.2 METHOD OF FFOWCS WILLIAMS AND HAWKINGS

To account for the presence of a moving solid body, an equation has been derived by Ffowcs Williams and Hawkings. These equations will reduce the computational expense in comparison to the solution of Curle's analytical solution [12]. The Ffowcs Williams and Hawkings wave equation can be derived from the Navier-Stokes equations. The idea of this derivation is to force every variable to be zero inside a predefined volume. To achieve this, the wave equation should be modified in such a way that it is valid in the whole flow domain. This way the free field Green's functions can be applied to the inhomogeneous wave equation in the entire domain. This manipulation is done by multiplying the Navier-Stokes equations by the Heaviside step function. This function has the following properties

$$\begin{aligned} H(f) &= 0 \;\; for \;\; f < 0 \\ H(f) &= 1 \;\; for \;\; f > 0 \end{aligned} \tag{17}$$

This implies that $f < 0$ inside the body and $f > 0$ outside the body therefore in the fluid domain. The function f is a function of the x-coordinate. Now let control volume be denoted by V, enclose the solid body and denote the surface of the volume by S. Then function f must be chosen a such that

$$\begin{aligned} f(x) &< 0 \quad if \;\; x \in V \\ f(x) &= 0 \quad if \;\; x \in S \\ f(x) &> 0 \quad if \;\; x \notin V \end{aligned} \tag{18}$$

Now the Navier-Stokes equations are multiplied by the Heaviside function. This way the equations apply to the fluid domain and the variables inside the control volume are zero.

$$H(f)\left[\frac{\partial r}{\partial t}+\frac{\partial r u_i}{\partial x_i}\right]=0 \tag{19}$$

$$H(f)\left[\frac{\partial r u_i}{\partial t}+\frac{\partial}{\partial x_j}\left\{r u_i u_j - s_{ij}\right\}\right]=0 \tag{20}$$

Combining these two equations and using the isotropic relation $dp = c_0^2 d r$, we obtain the Ffowcs Williams and Hawkings equations given in (21).

$$\frac{1}{c_0^2}\frac{\partial^2 p'}{\partial t^2}-\frac{\partial^2 p'}{\partial x_i \partial x_j}=\frac{\partial^2}{\partial x_i \partial x_j}\left\{T_{ij}H(f)\right\}-\frac{\partial}{\partial x_i}\left\{\left[s_{ij}n_j+r u_i\left(u_n-v_n\right)\right]d(f)\right\}+\frac{\partial}{\partial t}\left\{\left[r v_n + r\left(u_n-v_n\right)\right]d(f)\right\} \tag{21}$$

Here *u* is the velocity of the fluid and *v* is the velocity of the surface. For both velocities the subscript *i* indicates the direction of the velocity and subscript *n* indicates the normal component. The *δ(f)* is the Dirac delta function, which appears from the gradient of the Heaviside function. In (21) again the sources of sound can be identified. The first term is the contribution by the quadrupoles in the volume as represented by the Lighthill stress tensor. The other two terms are due to the distribution on the control surface, because the *δ(f)* is zero except at the surface, f = 0. In Fluent the contribution of the volume integral is neglected. This means that the quadrupole contribution of the Lighthill stress tensor is automatically excluded from the calculation. We end up with (22).

$$\frac{1}{c_0^2}\frac{\partial^2 p'}{\partial t^2}-\frac{\partial^2 p'}{\partial x_i \partial x_j}=-\frac{\partial}{\partial x_i}\left\{\left[s_{ij}n_j+r u_i\left(u_n-v_n\right)\right]d(f)\right\}+\frac{\partial}{\partial t}\left\{\left[r v_n + r\left(u_n-v_n\right)\right]d(f)\right\} \tag{22}$$

The end result is quite simple. The first source term is often called the loading term, because it represents the sound generated by the forces on the body. The second term is referred to as the thickness noise, which is related to the time dependant fluctuation of the surface.

In the result presented in (22) the integration surface is of big importance. The surface should be chosen in such a way that it is valid to neglect the contribution of the Lighthill stress tensor. For flows with dominant acoustic regions, like the slat cove, this integration surface has to enclose the region so the contributions are taken into account. For many low Mach number flow it is valid to exclude the Lighthill stress tensor, see Pan [10].

If the surface is chosen as the surface of the solid body, which is of course impermeable and non-moving, the relation for the sound production is further simplified to (23). As can be seen the forces of the fluid on the body are the acoustic sources.

$$\frac{1}{c_0^2}\frac{\partial^2 p'}{\partial t^2}-\frac{\partial^2 p'}{\partial x_i \partial x_j}=-\frac{\partial}{\partial x_i}\left\{\left[s_{ij}n_j\right]d(f)\right\} \tag{23}$$

Earlier reports, like Singer et al. [14], show that taking an off-body surface does not directly imply that the acoustic results are better, even though it is physical more complete. Flow fluctuations on the body may dissipate and disperse numerically by the CFD computation before reaching the off-body surface. This will be verified with the cylinder test case by performing a simulation with an on-body integration surface and an off-body integration surface, as is described in section 3.2.1.

Relation (23) can now be calculated by means of free field Green's functions in the same way as the Curle's solution. The result is the pressure fluctuation generated by the unsteady forces.

$$p'_L(x,t)=\frac{1}{4p\,c_0}\iint_S \frac{\left(x_i-y_i\right)n_i \partial s_{ij}\left(y,t_e\right)}{R^2 \partial t_e} \tag{24}$$

where the subscript *L* denotes the pressure perturbation produced by the loading term.

3. RESULTS

3.1 BENCHMARK SIMULATIONS WITH A CIRCULAR CYLINDER

The flow around a cylinder with diameter d = 1.9 cm under a freestream velocity of U_∞ = 69.19 m/s at standard sea level conditions is calculated. These conditions correspond to a Reynolds number of about Re_d = 90,000. The geometry and mesh details of these simulations were discussed in previous sections. All simulations of the present work were performed on a Windows operated PC with an AMD Athlon 64 4000+ (2.42 GHz) processor and 2 GB RAM memory. This Section first discusses the aerodynamic and aeroacoustic validation quantities. Then the results of the comparative simulations are presented. At the end of this Section the results of the best simulation will be presented in more detail and some conclusions will be drawn in regard to the follow-up simulations. The timestep of the simulations was 5 x 10^{-6} and the total time 0.2 s.

To perform a qualitative analysis of the results, some appropriate flow quantities have to be chosen to use as comparative tools. These quantities must be easily accessible and comparable. Even more important is that good experimental data about them has to be available. In the next sections this is discussed for both the aerodynamic and aeroacoustic side of the problem. The raw Sound Pressure Level (SPL) data exported from Fluent is a very noisy signal. This data is smoothed using a locally weighted least squares quadratic polynomial technique which is robust in the sense that is resistant to outliers. The same technique is used for smoothing the Fast Fourier Transformation (FFT) of the raw C_l data. The smoothed data is used to obtain the validation quantities. The aeroacoustic data is sampled from receiver 1, the upper microphone (Fig. 11).

3.1.1 AERODYNAMIC AND AEROACOUSTICS REFERENCE VALUES

The aerodynamic flow properties that will be used to qualify the simulation results are the mean drag coefficient C_d, root-mean-square (RMS) drag coefficient $C_{d'}$, the mean lift coefficient C_l, the RMS lift coefficient $C_{l'}$ and the Strouhal number St. These quantities are defined by

$$C_d = \frac{D}{q_\infty d} \qquad C_{d'} = \frac{D'}{q_\infty d} \qquad C_l = \frac{L}{q_\infty d} \qquad C_{l'} = \frac{L'}{q_\infty d} \qquad St = \frac{f_s d}{U_\infty} \tag{25}$$

In Figure 7, the drag coefficient of a circular cylinder is given for a wide range of Reynolds numbers. It is taken from Anderson [1]. As can be seen, the Reynolds region of our interest lies in a plateau of nearly constant Cd = 1.2.

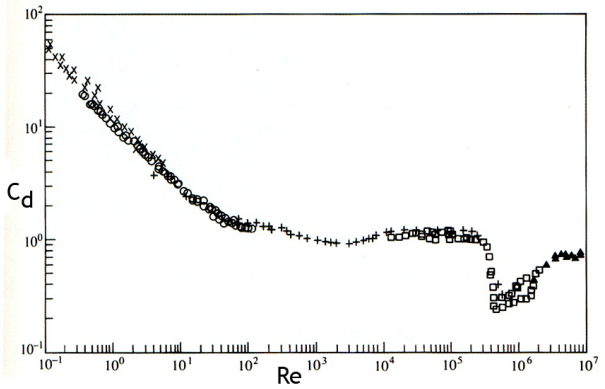

Above Left. Figure 7 – Drag coefficient vs. Reynolds number for a circular cylinder.

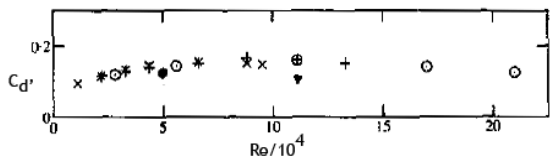

Above Right. Figure 8 – RMS drag coefficient as function of Reynolds number.

The experimentally determined value of $C_{d'}$ can be found in Figure 8, which was presented by West [19]. The reference value for Re_d = 90,000 is then $C_{d'} \approx 0.18$.

In cylinder flow the mean lift coefficient is zero for obvious reasons. Experimental research of time-varying lift of cylinder flow has focused on determining the RMS of the lift fluctuations. Despite a lot of efforts however, researchers have yet not been able to agree about correct value for $C_{l'}$ (Re). In Figure 9, which is taken from Norberg [9], we consider $C_{l'} \approx 0.45 - 0.6$ for the current case under study.

The vortex shedding Strouhal number can be found in Fig. 10 to be $St_{vs} \approx 0.19$. The figure was taken from Norberg [9].

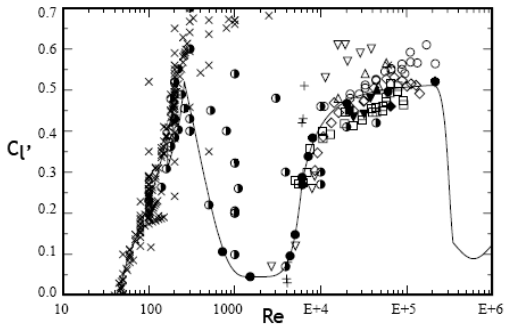

Figure 9 - RMS lift coefficient as a function of Reynolds number.

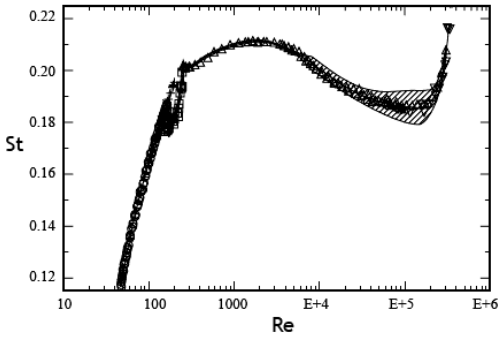

Figure 10 - Strouhal number as a function of Reynolds number.

The aeroacoustic property of interest is the Sound Pressure Level (SPL) at some defined receiver locations. In the simulations these locations were chosen as to replicate the setup used by van der Kooi [18], which is depicted in Figure 10. Van der Kooi measured the SPL of a smooth cylinder at several Reynolds numbers. His results are displayed in figure 12. The 73 m/s line corresponds to a Re_d = 100, 000. The properties of most interest are the peak SPL and the Strouhal number St_{ps} at which this occurs. The interpolated peak SPL for Red = 90, 000 is found to be around 107 dB at St ≈ 0.21.

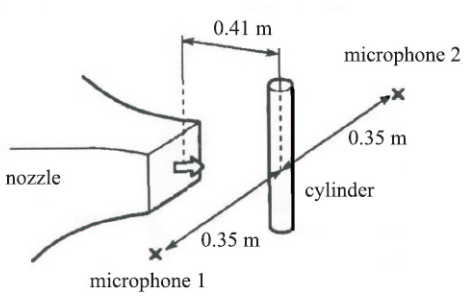

Figure 11 – Experimental set-up by van der Kooi [18].

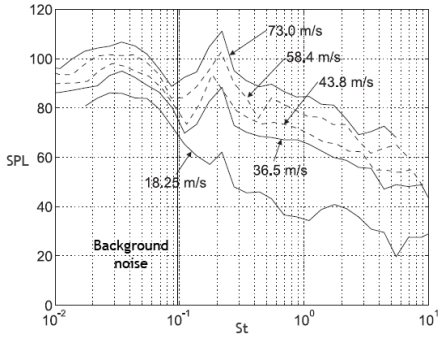

Figure 12 - Sound Pressure Level as a function of Strouhal number.

Table 1 – Summary of reference values for the benchmark cases.

Variable	Value
C_d	1.2
$C_{d'}$	0.18
C_l	0
$C_{l'}$	0.45-0.60
St_{vs}	0.19
SPL (dB)	107
St_{ps}	0.21

3.1.2 COMPARING SGS MODELS

The main conclusion from the literature study was that the influence of the SGS models on the results is quite small. To get some hands-on experience with the performance of the models it was however decided to make a comparison nonetheless. When using the LDK model, the authors were not able to achieve convergence of the subgrid kinetic energy transport equation involved with this model. Therefore this model was omitted from further use. All simulations were run with Interactive Time Advancing (ITA) time stepping and SIMPLEC pressure-velocity coupling. In the ITA scheme, within a given timestep, all the equations are solved in a blockwise loop until the convergence criteria for all equations are met. Thus, advancing the solution by one timestep normally requires a number of global iterations. With the iterative scheme, non-linearity of the individual equations and couplings between equations are fully accounted for, eliminating the splitting error, which is caused by the segregation of the equations. This is usually overkill, because the overall solution accuracy is limited by the time discretization error.

In Table 2 the results of the comparison are displayed. The differences between the results are not very big. All models and Smagorinsky in particular seem to overpredict the magnitude of the vortex shedding, because of which all values are a bit too high. Especially the fluctuation coefficients $C_{d'}$ and $C_{l'}$ are quite drastically overestimated. The overall picture shows a coarse agreement with the benchmark values. WALE and LDS are found to be around 30% more expensive. The shedding frequency and the Sound Pressure Level are quite well approximated by the WALE simulation. For this reason, WALE is used for all other simulations performed in this study.

Table 2 – Comparison of SGS models.

Quantity	BM	Smagorinsky	LDS	WALE
C_d	1.2	1.486	1.433	1.525
$C_{d'}$	0.18	0.3409	0.3407	0.4555
C_l	0	0.0559	-0.0009	0.0007
$C_{l'}$	0.45-0.6	1.344	1.127	1.131
St_{vs}	0.19	0.2363	0.2258	0.1860
St_{ps}	0.21	0.2420	0.2283	0.2039
SPL [dB]	107	112.6	111.1	109.4
CPT [s]		1.07	1.37	1.35

3.1.3 COMPARING MESHES

One of the most important aspects of every numerical analysis is of course the mesh choice. In this comparison our attention is focused to the influence of modifying the mesh. Particularly the influence of wall treatment on the final result is investigated. The results of the normal grid simulation (which uses a wall function) are compared to those obtained using finer meshes, which ought to resolve the full boundary layer structure. The simulations are denoted as coarse, intermediate and fine. All simulations were run with Non-Interactive Time Advancing (NITA) time stepping and WALE SGS model. The NITA scheme performs a single global iteration per timestep. There are subiterations performed on the segregated equations within each time step, but the outer iteration (velocity-pressure iteration) is performed just once, hence the term *non-iterative*. This approach effectively drives the splitting error to the time discretization error and is nonzero. It must be noted that this method is only applicable for incompressible or weakly compressible flow, which is the case in the problem at hand. The big advantage of the NITA method is that it gives a significant decrease in computational expense. Some sources give examples of a reduction in computational expense of 75% when using NITA instead of ITA.

The results are displayed in Table 3 below.

Table 3 – Results for different mesh sizes. BM is the reference value.

Quantity	BM	Coarse	Intermediate	Fine
C_d	1.2	1.202	0.6015	0.9788
$C_{d'}$	0.18	0.2902	0.1162	0.2332
C_l	0	0.0012	0.0352	0.0473
$C_{l'}$	0.45-0.6	0.9001	0.6232	0.9534
St_{vs}	0.19	0.2045	0.3027	0.2463
St_{ps}	0.21	0.2222	0.3038	0.2424
SPL [dB]	107	110.4	110.4	109.2
CPT [s]		0.55	0.51	1.78

The results of the finer meshes are somewhat disappointing. The finest mesh gives better results than the intermediate one but is in no way better than the coarsest mesh. In the intermediate case two different vortex shedding frequencies could be distinguished. Clearly the true physical vortex shedding is not captured properly in this simulation. As observed by Piomelli [11] and Templeton [16] the near-wall vortical structures are of a very small scale, but nevertheless dynamically important. SGS models are found to be incapable of capturing the correct physics associated with these small structures. This means excessively fine grid resolutions have to be adopted when using this so-called *solve-to-wall* approach. Refining the grid in wall-normal direction creates cells with a bad aspect ratio, which in LES is found to give bad results. This means that all directions have to be refined, because of which the necessary resolution in fact approaches that of a full DNS simulation. In both the fine mesh simulations Fluent adopts the *solve-to-wall* approach, although the resolution is not nearly as high as necessary to capture the correct physics. This is probably the main reason for the failure of the finer mesh simulations. The wall-modeling technique used in conjunction with the coarse grid seems to perform adequately and will therefore be adopted in the other more complex cases. It should be noted that the comparison of CPT between the coarse and finer grids is not really representative, because the structure of the grids (and their qualities, which influences convergence) differs somewhat. It is however clear that in the case the meshes are structurally comparable, a lower number of cells results in a lower expense.

3.1.4 COMPARISON OF INTEGRATION SURFACE

In this section the influence of the integration surface used in conjunction with the Ffowcs Williams and Hawkings Equation (24) will be investigated. The mesh and integration surfaces used for the simulations were discussed previously. The results of the simulations are displayed in Table 4 below. Because the only difference between the simulations is found in the acoustics, only these quantities are given.

Table 4 – Comparison of integration surface.

Quantity	BM	On-cylinder	Off-cylinder
St_{ps}	0.21	0.2087	0.2087
SPL [dB]	107	106.4	106.2

It appears that the assumption that the sound generated in the off-body region is negligible is indeed valid in this case. The choice of integration surface hardly alters the outcome. For the slatted-airfoil configuration this is not necessarily the case and will be discussed later.

3.1.5 GRAPHICL VISUALIZATION AND SPL

The results presented here are considered to be the best ones (Table 5 and 6). A nice visualization of the vortex shedding behavior is formed by a filled contour plot of the velocity magnitude, as given in Figure 13. The vortex shedding character is clearly visible from the low/high velocity pairs, which indicate that there is an alternating sequence of clockwise rotating vortices shedded from the upper side and counterclockwise rotating vortices shedded from the lower side.

Table 5 – Aerodynamic coefficients for the circular cylinder.

Quantity	BM	NITA
C_d	1.2	1.202
$C_{d'}$	0.18	0.2902
C_l	0	0.0012
$C_{l'}$	0.45-0.6	0.9001
St_{vs}	0.19	0.2045

The sound pressure level spectrum produced by this simulation is displayed in Figure 14. The included experimental data was obtained from an interpolation of the 73.0 m/s and 58.4 m/s datasets of van der Kooi to correct for the deviating Reynolds number. The agreement with the experimental data is very good. The peak SPL and its corresponding Strouhal number are predicted fairly well. The global deviation is however around 12 dB, which is considerable.

Table 6 – Aeroacoustics results for the circular cylinder.

Quantity	BM	NITA
St_{ps}	0.21	0.2222
SPL [dB]	107	110.4

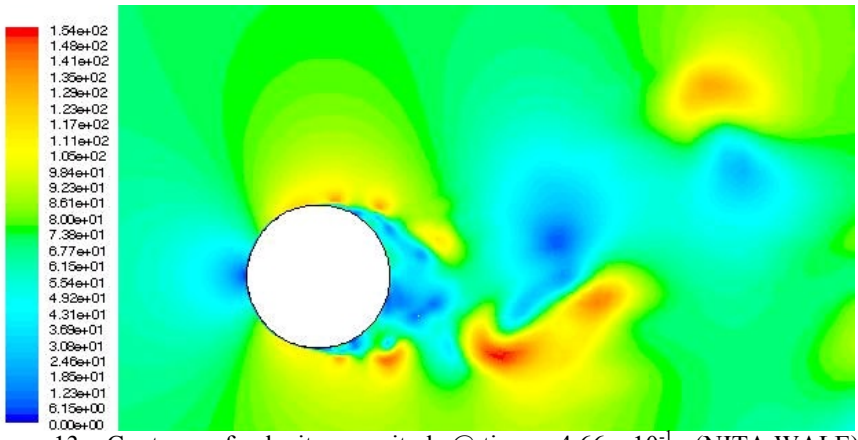

Figure 13 – Contours of velocity magnitude @ time = 4.66 x 10^{-1} s (NITA,WALE).

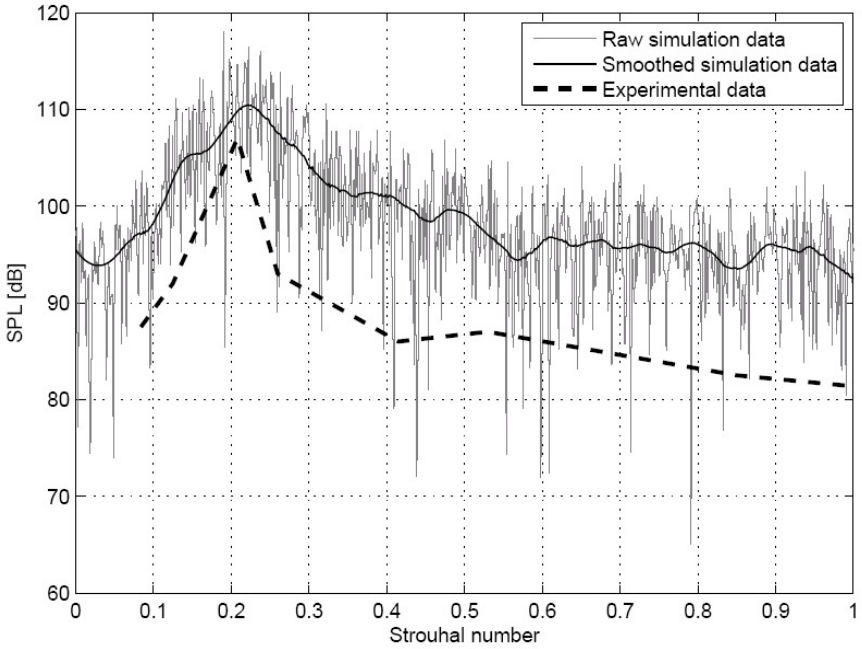

Figure 14 – Sound pressure level at receiver 1.

3.2 SLATTED-AIRFOIL CONFIGURATION

The geometry and mesh of the high-lift airfoil is shown in Figs. 15 and 16. As can be seen in the Fig. 16, another surface is defined by the dashed line. This surface was used for the computation of the sound radiation and encloses the slot. A report of Andreou [2] is used for validation of this case. The aeroacoustic measurements are done on the tunnel floor with an array of microphones. The vertical distance between the microphone array and the wing is 0.6 m. The use of two different arrays resulted in a measurement with a frequency range between 2 kHz and 20 kHz. The validation of the simulation will be done in this bandwidth. The acoustical emission outside this bandwidth will be discussed as well. Especially the contribution in the audible range will be looked at. Three measurements are done to distinguish the effect of the angle of attack, α = 6°, 10°, and 16°. The report of Andreou does not only discuss the aeroacoustics of the configuration but also provides aerodynamic data. Because of the influences of the tunnel walls, this data is corrected using lift-interference and blockage corrections as can be found in ESDU.

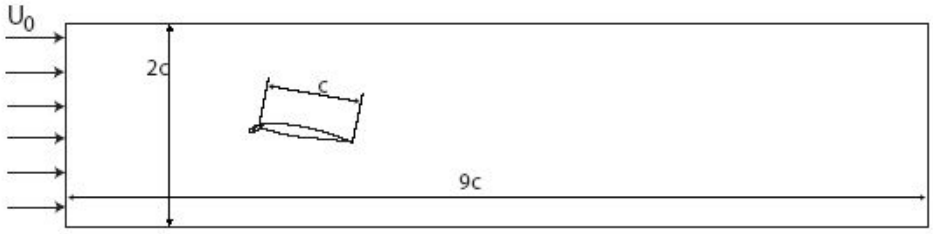

Figure 15 – Domain for the slatted-airfoil case.

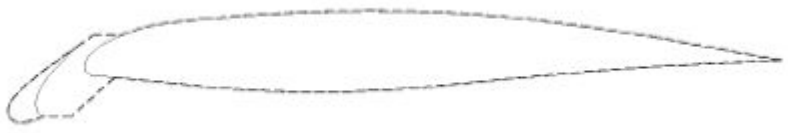

Figure 16 – Closer look at the slat airfoil configuration.

3.2.1 AEROACOUSTICS DATA

The report by Andreou focuses on the determination of the sources of sound. The setup with the microphone array is capable of locating the sources of sound. As can be read in the report, the slat is the main noise contributor. Fig. 17 shows the experimental data for different frequencies at an angle of attack of 6°. The leading and trailing edge of the airfoil are indicated by the thick black lines. It is clear that the slat is the main contributor to the noise generation of the total configuration.

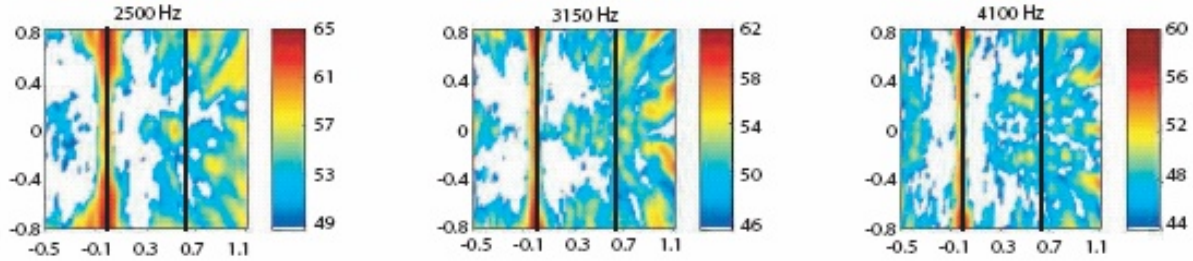

Fig. 17 – Sound pressure pattern for $\alpha = 6^o$.

The source location can also be determined with Fluent. This is done by plotting the source dipole strength on the surface of the slat and airfoil. Integrating this term over the surface will give the contribution of all the sources on the surface to a specified observation point. The source dipole strength is given in Fig. 18 for $\alpha = 6^o$. The slat, the slot and the leading-edge region of the main wing are the main sources of sound. The dipole strength on the upper surface of the main wing is not measured in the experiments and therefore does not show in Fig. 17. The source dipole strength for the case of 16^o angle of attack in particular is very strong at the upper surface. This indicates that there is a lot of noise radiation upwards, which was unfortunately not tested in the wind tunnel. Also the sound pressure level at the tunnel floor was measured in the experiment. Our corresponding acoustic simulation was run with eight receivers at the lower tunnel floor, with the receivers 0.1 m apart. SPL was calculated at these receiver points. It was found that there is not a significant difference between the receivers. Therefore, the sound pressure level of the receiver below the slat is used for the comparison. In Fig. 19 the experimental SPL data is given for different angles of attack.

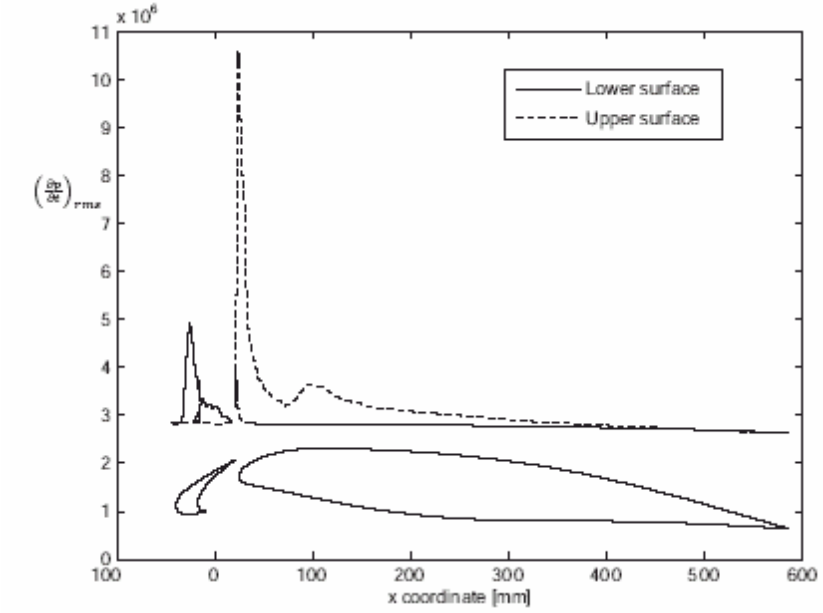

Figure 18 – Source dipole strength along airfoil surface.

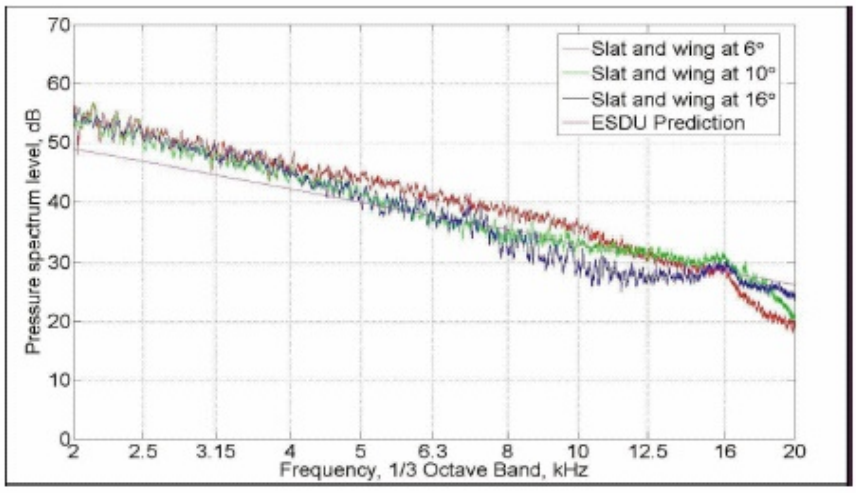

Figure 19 – Experimental SPL for $\alpha = 6^o$, 10^o, and 16^o.

The SPL data calculated from the simulation is given in Fig. 20. The rough data is smoothed using the same weighted least squares method as the one used in the previous chapter. In that Figure the dashed line is a simplification of the experimental data, given in Fig. 19. It can be observed that the simulation overestimates the sound production by 5-10 dB. In aircraft design envisaging noise reduction, a usual target is the SPL prediction within an error margin of 10 dB, so this result is satisfactory. Furthermore it is important that the trend and specific peak frequencies are captured properly. It is noted that the trend is captured well up to a frequency of about 10 kHz. The decrease of accuracy in the high frequency zone can be accounted for the mesh size. Further study of some literature showed that often the smallest wavelength is resolved on ten grid points instead of five. This means that the mesh should be refined by a factor of about two, which would lead to a very large mesh. To keep the computational expense at a reasonable level, the refinement is only applied to the slot region, because this region is most responsible for the sound production. The results of this simulation are shown in Figure 20.

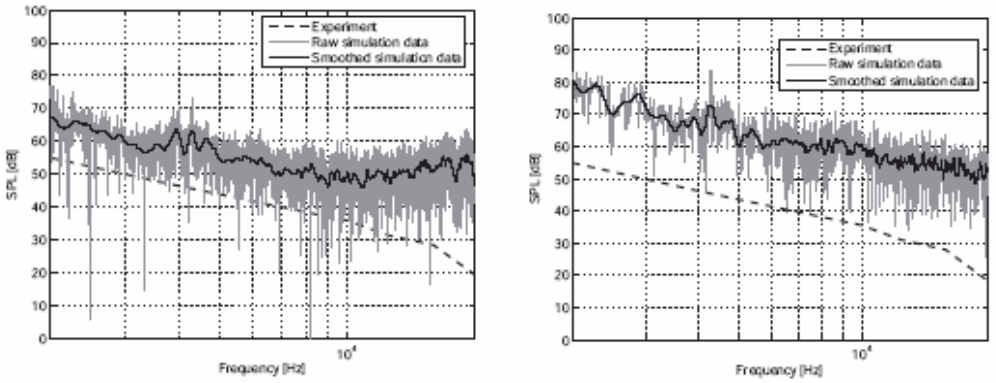

(a) Initial grid (b) Refined grid

Figure 20 – Experimental and computed SPL data for $\alpha = 6^o$.

As can be seen the results for the finer grid are not better. Especially in the low frequency region the simulation lacks accuracy. One could say that the trend is captured better with the finer grid, but this is just an effect of the increased SPL deviation at low frequencies. We can therefore conclude that refining only the slot region is not enough to increase the accuracy of the sound emission prediction. The refining has to be extended towards the source surfaces and especially to the lower surface of the slat. It is believed that refinement in these regions will increase the accuracy, but because of the lack of time no further simulations to investigate this suspicion were performed. Again caution has to be taken with these refinements because the $y+$ value should stay above 20 and the aspect ratio of the elements needs to stay good.

As earlier discussed, the integration surface is introduced in order to capture more physics and to obtain a better simulation of the sound production. In the benchmark case it is proven that for the cylinder the results did not differ much. For the simulation of the slatted-airfoil configuration two integration surfaces were used to calculate the sound emission. The results of this calculation are shown in Fig. 21. For these simulations the refined grid was used to avoid dissipative effects in the slot region. The use of two separate integration surfaces which are at a close distance is physically not realistic. In the region between the surfaces reflection plays a dominant role, but is not accounted for by the method of Ffowcs Williams and Hawkings. By enclosing this whole reflective region, this problem is avoided and reflection is taken into account. The on-body surface is indeed found to perform somewhat worse, when looking at the trend line, as can be seen in Figure 21.

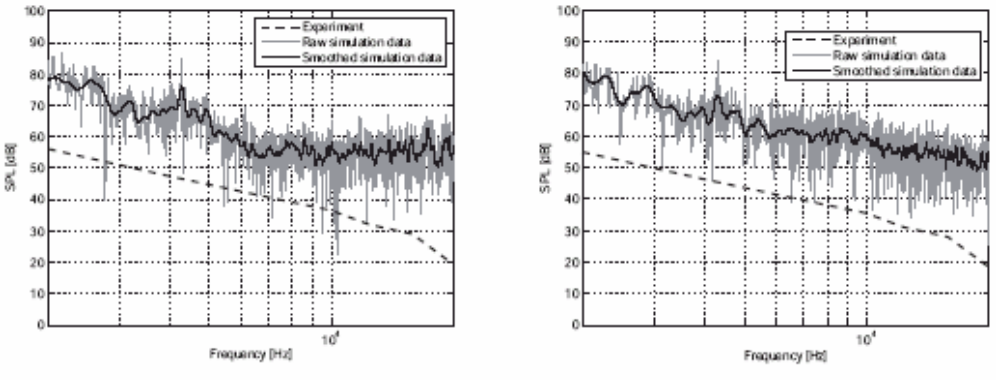

(a) On-body integration surface (b) Off-body integration surface

Figure 21 – Sound generation from different integration surfaces.

In the experiment of Andreou only the frequencies between 2 kHz and 20 kHz were measured. The trend of the numerically obtained SPL however shows that low frequencies are most dominant in the spectrum. From an engineering point of view the bandwidth of interest extends to the low frequencies up to 20 Hz. The simulation was run long enough to also capture even lower frequencies; these results are shown in Figure 22. The region left out of the measurements of Andreou is indeed very interesting. Especially the region between 200 Hz and 1000 Hz has a relatively high SPL. This region diminishes when the angle of attack is raised. This phenomenon can possibly be ascribed to the boundary layer instability and the vortex shedding initiated from the instability at the lower slat surface. It only occurs at low angles of attack as will be clarified in the aerodynamic section.

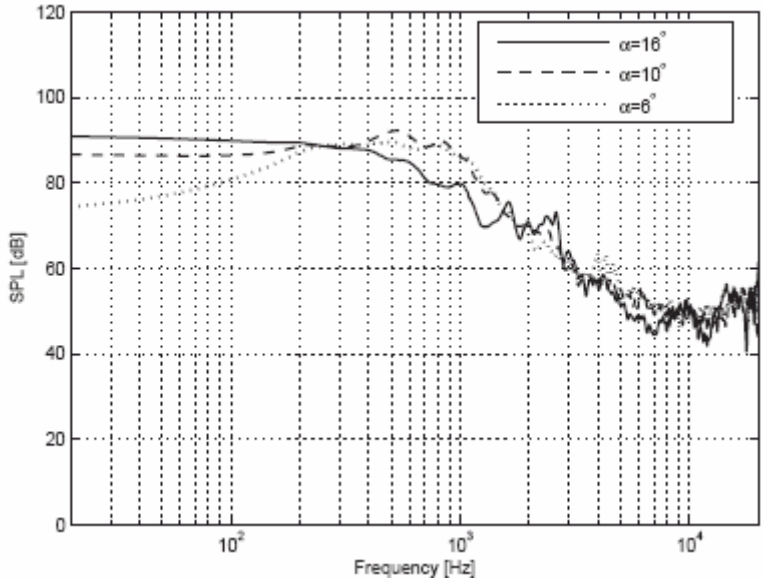

Figure 22 – SPL for all angles of attacks in the audible range.

The same phenomenon causes the high source dipole strength on the lower slat surface, as shown in Fig. 18. The instability in the boundary layer causes pressure fluctuations on the surface, which translates to sound emission. As the angle of attack is raised the boundary layer instability will occur at the upper surface of the slat.

The source dipole sound is caused by the instability and the formation of vortices in the boundary layer. These instabilities can be visualized by plotting the pressure distribution in the flowfield at a certain instant in time. This distribution is given in Fig. 23 as the relative pressure deviation from the freestream pressure. It is clear that the instability occurs at the upper surface of the main element. These fluctuations were also visible in the source dipole strength plot in Fig. 18. There is also a large recirculation area visible in the slot. This region is feeded by the two shear layers which originate from the slat trailing edges. Some additional detail plots of vorticity in the slot region are displayed in Fig. 24.

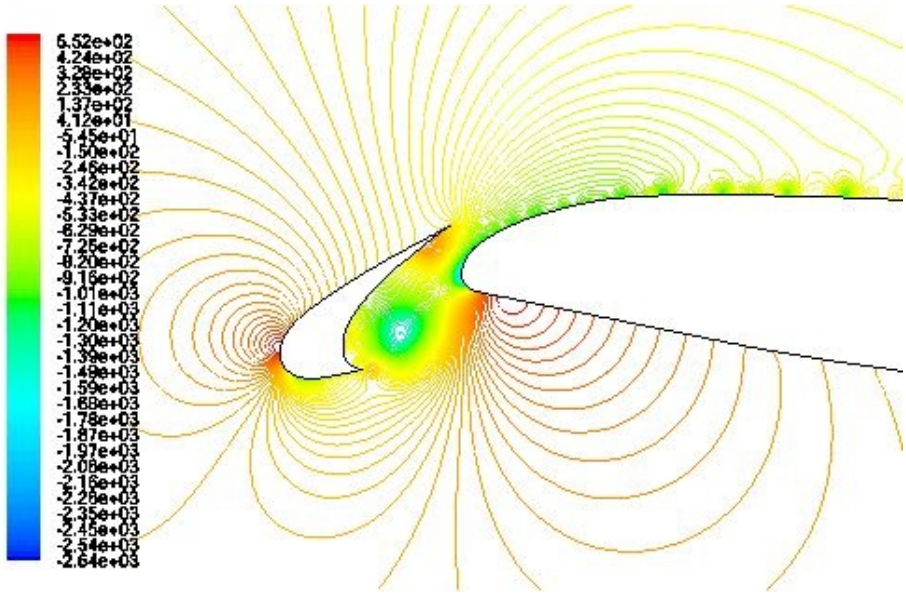

Figure 23 – Iso-pressure contour lines for $\alpha = 6^{o}$ (Pa).

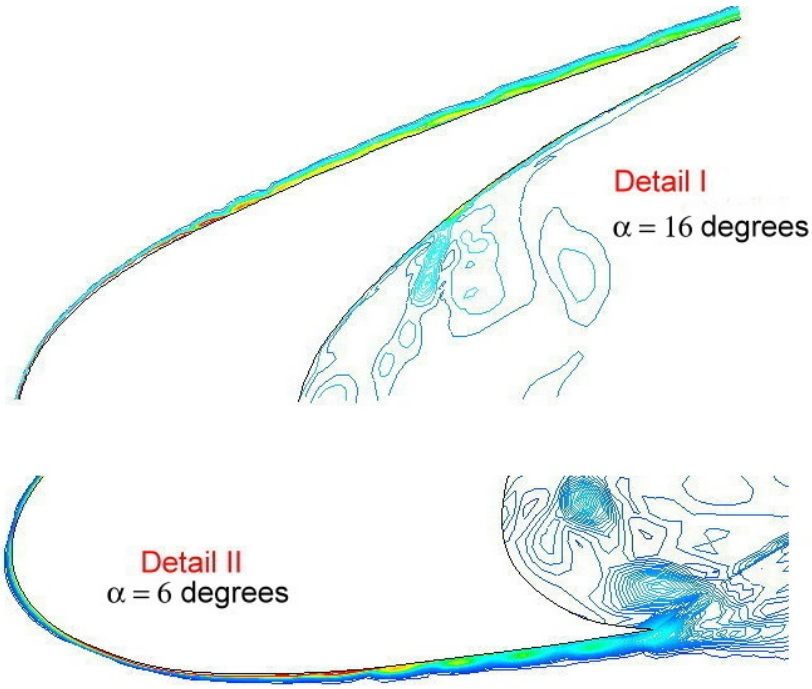

Figure 24 – Iso-vorticity plots for the slatted-airfoil configuration.

The boundary layer separation on the slat can be related to the pressure distribution on the surface. If the pressure gradient is negative the flow is accelerated and the boundary layer will be stretched. This damps the instability and prevents separation of the boundary layer. On the other hand if the pressure gradient is positive, separation can occur and therefore the pressure coefficient gives a good estimation for boundary layer separation. For one instant in time the pressure coefficient along the surface is given in Fig. 25. The pressure fluctuation on the lower surface of the slat is also clearly visible. Again these results comply very well with the results found before. For graphical purposes the slat geometry given in the Figure is stretched and does not comply with the real geometrical dimensions.

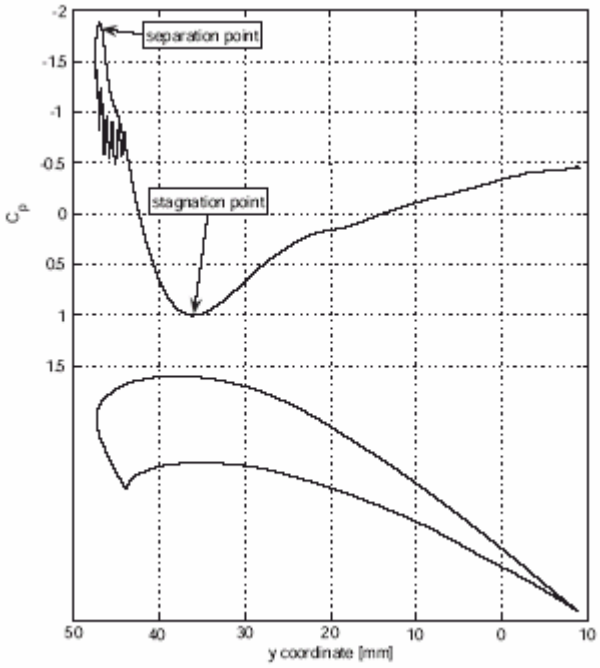

Fig. 25 – C_p Distribution on slat surface ($\alpha = 6^o$).

The same can be done for the main elemnt. Here the instability occurs at the upper surface. The pressure fluctuations are present over the whole upper surface (Fig. 26). The wavelength of the fluctuations increases when traveling towards the trailing edge. This indicates that small eddies are generated near the leading edge and are convected with the flow while increasing in size. As stated before, the scale of the eddies is roughly proportional to the wavelength of the sound

radiation. This means that the emission near the leading edge is relatively high-frequent and near the trailing edge low-frequent. The scales of the eddies can be visualized using iso-pressure contours. This is done in Fig. 27. On the lower surface a negative, or adverse, gradient is maintained over almost the whole surface, except for the region from half the chord length up to the trailing edge. Here the pressure shows some harmonic oscillations around a nearly constant value. These fluctuations are however very small. They are caused by small eddies that are shedded from the point where the geometry changes fairly suddenly and convected along the surface.

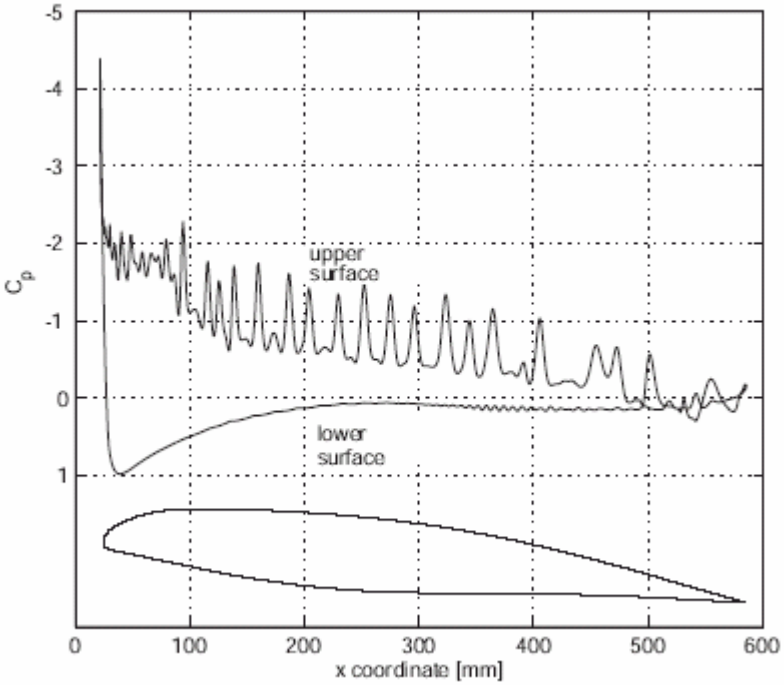

Figure 26 – C_p distribution on main element at $\alpha = 6^o$.

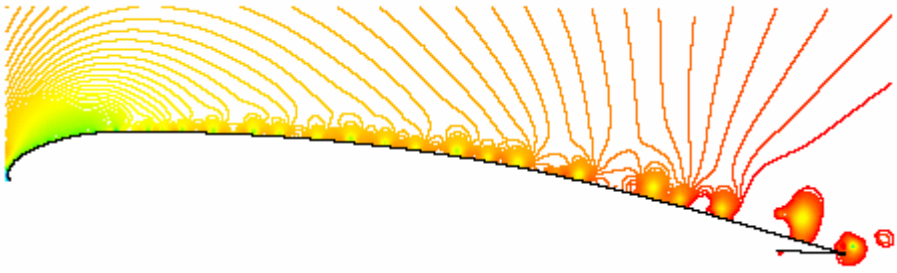

Figure 27 – Iso-pressure contours on the main element at $\alpha = 6^o$.

4. CONCLUDING REMARKS

The study of the models available in Fluent has proven its efficiency. The effort that had to be put in the benchmark simulations was reduced by a rather thorough investigation of the literature. Because of this, the limitations of the used models were known and therefore the problems arising during the simulations could be solved quite effectively.

A reasonably good agreement with experimental results has been obtained with the benchmark simulation. The aerodynamic and aeroacoustic quantities could be obtained quite accurately. The coefficients that describe the time-varying behavior of the lift and drag fluctuations are however poorly predicted. As stated before, this a known problem. Even experimental research in this area has proven to be hard enough as it is. Especially the lift fluctuation shows a lot of disagreement when comparing multiple studies.

The vortex shedding and general flow structure is found to be captured quite properly. It is hard to qualify this statement because of the unstable character of the vortex street associated with high Reynolds number. The overall picture seems to suggest however that the flow is resolved fairly accurately. The reasonably good aeroacoustical results strengthen this feeling, because an accurate flow solution is absolutely crucial to achieve these. The peak SPL and dominant Strouhal

number were predicted well, although the global trend in the SPL spectrum was overestimated by ± 12 dB. This fairly large deviation is most likely caused by the defect of neglecting relieving 3D effects when performing a 2D simulation. Another possible cause could be found in numerical problems involved with the Ffowcs Williams and Hawkings method. There have been reports of problems with the accurate evaluation of the pressure gradient that is used in the method.

The wall treatment was found to be especially important. The *solve-to-wall* approach did not work at all. It was found that the mesh needs to be very fine in the turbulent regions of the flow, but coarse enough to facilitate the use of the wall function.

A critical note must be made though. The big differences between the outcomes of several simulations cause some doubts about the method. Changes in the mesh or the use of another SGS model can drastically alter the results. It is found that LES is highly sensitive to the simulation parameters in this kind of flow. Because of this, we cannot be absolutely sure that the simulation done with NITA and WALE was not just a lucky one. It is well known that 2D simulations tend to overpredict the aerodynamic forces, see for example Mittal [8]. Because the drag coefficient obtained from the best simulation was on the spot, we have to be a bit distrusting. The overprediction was apparently corrected by a damping numerical or model mechanism. However, because we do not have more information to go by, we will stick with WALE.

According to our experience in running the simulations, we provide a recipe for successful simulations with Fluent

- A grid that is very fine in the turbulent regions, but has $y+$ value along the object surface of at least 20 to facilitate wall treatment.
- NITA timestepping in combination with FSM pressure-velocity coupling.
- WALE subgrid-scale model.

The location of sound sources were estimated accurately, analysis of the simulation data showed a good compliance with the experimental data. The acoustic model of Ffowcs Williams and Hawkings allowed to take an off-body integration surface. This only proved to play an important role in geometries that contain multiple sections, between which complex acoustical behavior takes place. The integration surface could be used to enclose the region in which reflection was present. In the high-lift airfoil case this approach was found to give somewhat better results.

The sources of sound were found to be quite well predicted. Correcting for an overprediction of about 10 dB then gives a fairly good idea of the overall sound production of the configuration. It should be noted of course that we can not qualify this statement for higher Reynolds number or more complex configurations.

5. BIBLIOGRAPHY

[1] Anderson, J. D., *Fundamentals of Aerodynamics*. McGraw-Hill, 2001.

[2] Andreou, C., Graham, W., and H. Shin, H. C., "In Aeroacoustic Study of Airfoil Leading Edge High-Lift Devices," 27th AIAA Aeroacoustics Conference, AIAA/CEAS, May 2006.

[3] Colonius,T. and Lele, S. K.. "Computational Aeroacoustics: Progress on Nonlinear Problems of Sound Generation," Progress in Aerospace Sciences, (40):345–416, 2004.

[4] Fluent Version 6.2 User's Guide, Fluent Inc., New Hampshire, January 2005.

[5] Guermond, J. L., Oden, J. T., and Prudhomme, S., "Mathematical Perspectives on Large Eddy Simulation Models for Turbulent Flows." Journal of Mathematical Fluid Mechanics, 6:194-248, 2004.

[6] Layton, W. J., A Mathematical Introduction to Large Eddy Simulation, VKI Lecture Notes, 2002.

[7] Lighthill, M. J., "On Sound Generated Aerodynamically I. General Theory," Proceedings of the Royal Society of London, 211(1107):564-587, May 1952.

[8] Mittal, R. and Balachander, S., "Effect of Three-dimensionality on the Lift and Drag of Nominally Two-dimensional Cylinders," Physics of Fluids, 7(8):1841-1865, August 1995.

[9] Norberg, C., "Fluctuating Lift on Circular Cylinder: Review and New Measurements," Journal of Fluids and Structures, 17:57-96, 2003.

[10] Pan, Y. S., "Perturbation Solution of the Navier-Stokes Equations and its Relation to the Lighthill-Curie Solution of Aerodynamic Sound," Journal of the Acoustical Society of America, 58(4):794-799, October 1975.

[11] Piomelli, U., "Large-Eddy Simulation: Present state and future perspectives," 36th Aerospace Sciences Meeting and Exibit, January 1998.

[12] Rienstra, S. W. and Hirschberg, A., *An Introduction to Acoustics*, Eindhoven University of Technology, 2004.

[13] Schlichting, H., *Boundary-Layer Theory*. McGraw-Hill Inc., 1979.

[14] Singer, B. A., Lockard, D. P., and Brentner, K. S., "In Computational Aeroacoustic Analysis of Slat Trailing-Edge Flow," 5th AIAA/CEAS Aeroacoustics Conference, pages 1-11, AIAA/CEAS, May 1999.

[15] Tannehill, J. C., Anderson, D. A., and Pletcher, R. H., *Computational Fluid Mechanics and Heat Transfer*. Taylor and Francis, 1997.

[16] Templeton, J. A., Wang, M., and Moin, P., "Towards LES Wall Models Using Optimization Techniques," Centre for Turbulence Research Annual Research Rebriefs, pages 189-200, 2002.

[17] Tennekes, H. and Lumley, J. L., A First Course in Turbulence. The MIT Press, 1985.

[18] van der Kooi, J. T., "An Experimental Study of Aolean Tones and Trailing-edge Noise," Master's Thesis, University of Twente, October 2006.

[19] West, G. S., "Measurements of Fluctuation Pressures and Forces on a Cylinder in the Reynolds Number Range 10^4 to 2.5 x 10^5," Journal of Fluids and Structures, 7:227-244, 1993.

5. RESPONSIBILITY NOTICE

The authors are the sole responsible for the content of this paper.